ROYAL SOCIETY
OF CHEMISTRY

PAPER

Check for updates

Anodized SLM Ti6Al4V surfaces: influence of surface characteristics on NTs growth and resulted surfaces properties†

Marie-Joséphine Crenn, [ID] *[abf] Lanig Lefort, [ID] [f] Rémy Pires Brazuna, [ID] [c] Pierre Dubot, [ID] [c] Marie-Laurence Giorgi[d] and Patrice Peyre [ID] [e]

TiO_2 nanotubes (NTs) obtained *via* electrochemical anodization (EA) on conventionally machined titanium surfaces are reported to be promising for achieving mucointegration in dental implant therapy. Dental abutments, manufactured by selective laser melting (SLM), combined with thermal post-treatment, present a promising alternative to conventionally machined titanium. Based on an original protocol, this study aims to investigate how the characteristic microstructure of the $\alpha + \beta$ phases in post-heated SLM Ti6Al4V can influence the growth of NTs and the resulting physical and chemical surface properties. Ti6Al4V-SLM discs were fabricated, heat post-treated and mechanically polished. The samples were then subjected to EA under different voltage conditions (10, 20 and 30 V). The specimens' surfaces were characterized at the same location, before NTs formation by electron backscatter diffraction (EBSD), and after by scanning electron microscopy (SEM). Then, roughness and wettability were studied to determine how EA affects surface properties compared to conventionally machined and polished titanium surfaces without NTs (reference). Surface reactivity was evaluated through chemical analysis and collagen binding capacities. The self-organized TiO_2 layer was developed on the α phase only and the β phase was preferentially dissolved. The characteristic dimensions of the nanotubes (diameter, length and wall thickness), measured by SEM image analysis, increased proportionally with the rise in voltage but were not affected by the crystallographic orientation of the underlying α grain. Micro-roughness was the same for nanotubular and reference surfaces. Wettability was improved, as was surface reactivity towards collagen, which may contribute to improved bioactivity of titanium surfaces in dentistry.

a Innovative Biomaterials and Interfaces Research Unit - URB2i. Dental Faculty - Université Paris Cité, 9210, Montrouge, France. E-mail: marie-josephine.crenn@u-paris.fr

b Department of prosthodontics, Rothschild Hospital, 75012 Paris, France

c Institut de Chimie et des Matériaux Paris-Est (ICMPE) UMR 7182 CNRS - University Paris-Est Créteil 94320, Thiais, France. E-mail: pires@icmpe.cnrs.fr, pdubot@glvt-cnrs.fr

d Paris-Saclay University, CentraleSupélec, Génie des Procédés et Matériaux Unit, 91192, Gif-sur-Yvette cedex, France. E-mail: marie-laurence.giorgi@centralesupelec.fr

e PIMM Laboratory, Arts et Métiers Institute of Technology, CNRS, CNAM, HESAM University, 151 Bd de l'Hôpital, 75013 PARIS, France. E-mail: patrice.peyre@ensam.eu

f CRC UMR 1139, Team ''Oral Molecular Physiopathology'', University Paris Cité, 75006 Paris, France. E-mail: lanig.lefort@etu.u-paris.fr

† Electronic supplementary information (ESI) available. See DOI: https://doi.org/10.1039/d4tb00672k

Introduction

In implant dental therapy, nano-engineered titanium surfaces have gained considerable interest in optimizing both osseointegration and mucointegration. In this context, several surface modifications have been proposed to modify the surface properties of grade 5 titanium alloys (Ti6Al4V) preferentially used to fabricate prosthetic components. Among different techniques such as alkaline treatment, laser surface treatment, sol–gel, anodic oxidation, plasma electrolytic oxidation,[1,2] electrochemical anodization (EA) has gained interest. Indeed, EA is a relatively easy, cost-effective and reproducible technique[3] reported enhancing the bioactivity of the conventional "bioinert" Ti. This electrochemical technique based on a two-electrode system combined with different parameters (anodization time, voltage, and electrolyte composition) allows the formation of nanoscale features such as nanopores, nanotubes, nanopillars or nanograss.[4] When the synthesis variables are correctly defined, nanotubes (NTs) (open at the top and closed at the

11502 | *J. Mater. Chem. B*, 2024, **12**, 11502–11514

This journal is © The Royal Society of Chemistry 2024

bottom), with specific morphology (diameter, thickness wall, and length) may grow on the substrate.[5] The organized nanotube layer modifies the wettability, surface chemistry and topography which influences the behavior of human cells[6,7] including the cells surrounding the surface of the dental implant, *i.e.* osteoblast, fibroblast, and epithelial cells. Concerning NTs and osseointegration, it has been reported that NTs enhance osteoblast functions under *in vivo* conditions.[8] Regarding fibroblasts, several *in vitro* studies suggest that NTs positively influence adhesion, proliferation and function compared to conventional machined titanium surfaces[9,10] but only a few *in vivo* studies have investigated the response of soft tissues' behavior yet[11] showing that soft tissue healing around NT prosthetic components is similar to conventional surfaces after 12 weeks. NTs may also be used as a reservoir to contain drugs, proteins, and specific molecules[12] which may also be beneficial to epithelial cells[13] and prevent bacterial proliferation.[14] Of course, these results are simplified because each EA protocol produces its own surface, and there is no comparable anodized surface across the studies found in the literature. Nevertheless, these biological results regarding fibroblasts are very encouraging as they may fortify the soft tissue interaction with trans-gingival components,[15] very commonly represented by prosthetic components *i.e.* the abutment. It has also been reported that the NT layer improves chemical corrosion resistance, which is a major advantage in a corrosive environment such as the oral cavity.[16]

Until now, EA modification mainly concerns titanium surfaces obtained using traditional machining techniques and turned titanium, whereas abutment can now be constructed with additive manufacturing (AM) and more specifically by selective laser melting (SLM). To be used under intra-oral conditions, Ti6Al4V parts obtained *via* SLM must receive a post-thermal treatment to obtain mechanical properties required for dental applications.[17,18] This annealing modifies the alloy's crystalline structure by creating β domains along the characteristic α needles of the SLM process.

The scientific literature contains little information about the feasibility of anodizing Ti6Al4V devices derived from SLM AM Ti6Al4V. Regarding the SLM process, Xu *et al.* applied EA on the SLM grade II titanium substrate and showed a theoretically homogeneous surface in the presence of NTs measuring approximately 70–90 nm in diameter formed uniformly over the entire surface of the sample.[19] However, prosthesis components are preferentially made using Ti6Al4V and it has been reported that on polycrystalline Ti, the β phase prevents the formation of NTs.[20] Pruchova *et al.*[14] reported that the current lines created during electrochemical anodization may not be identical from one zone to another, depending on the chemical composition of the respective phases. Guo *et al.*[21] used grade V titanium powder (Ti6Al4V) to build specimens *via* the SLM process and reported that EA associated with high-temperature hydrogenation promotes the early adhesion and proliferation of fibroblasts. Even if the biological methodology is perfectly described, there is no information on how the characteristic microstructure inherent to SLM affects the growth of NT.

Furthermore, other studies report that the crystallographic orientation may also play a role in NT growth.[22] To the best of the author's knowledge, no study has yet attempted to link the influence of SLM microstructure and crystallinity on NT growth. However, the nanotubular layer created on titanium may, depending on its morphology, affect the surface properties such as roughness and wettability, which are known to play a crucial role in biological phenomena when a material is inserted into the human body.

Since the underlying substrate does influence how anodization will modify the surface, the objective of this present work, based on an original protocol, is to investigate how the microstructure of 3D printed Ti6Al4V and its crystallographic orientation influence the growth of NT and the resulting surface properties. To provide an initial insight into the bioactivity of the created surface, a collagen adsorption test is included in this work.

Experimental

Specimens' fabrication and phase characterization

Discs were manufactured using an SLM machine (SLM 125 HL) from Ti6Al4V ELI powder, grade 23 (CT powder range Ti64 F, carpenter additive), conventionally used in the biomedical field. Fig. 1(1) shows the SLM processing parameters. The objective of this optimization step was to obtain the lower porosity ratio which is essential to build prosthetic parts in dentistry. The particle size distribution had an average diameter of 37.19 μm (Fig. 1(2)). The orientation of discs during printing was chosen so that the surface of interest was oriented at 50° relative to the plate (Fig. 1(3)) to imitate the clinical condition of a printed transgingival component (such as dental abutment).

Postprocessing was performed according to the manufacturer's instructions in a furnace under an argon gas atmosphere. Heat treatment was performed by progressive heating at a rate of 10–12 °C min⁻¹, ending with a plateau at 880 °C for 2 hours. The specimens were finally cooled to room temperature in the furnace. As it was described, these post-processing steps are necessary to achieve the mechanical properties required for dental prosthesis production. To identify the phase before and after heat treatment, X-ray diffraction (XRD) analysis of the raw SLM sample was carried out. Patterns were acquired on an MPD PANalytical X'Pert Pro diffractometer, powered by a Philips PW3040/60 X-ray generator and equipped with an X'Celerator detector. Diffraction data were acquired by exposing the samples to X-ray radiation from a Cu-Kα anode, with a characteristic wavelength (l) of 1.5418 Å (voltage of 45 kV and current of 40 mA). Data were collected over a 2θ range of 5–160° with a step size of 0.0130° and a nominal time per step of 120 seconds, using the X'Celerator detector in scan mode. Phase identification and quantification, by the integration of the diffraction peaks relating to each phase, were performed using X'Pert PANalytical high score plus companion software in conjunction with ICDD powder diffraction file 2, ICDD powder
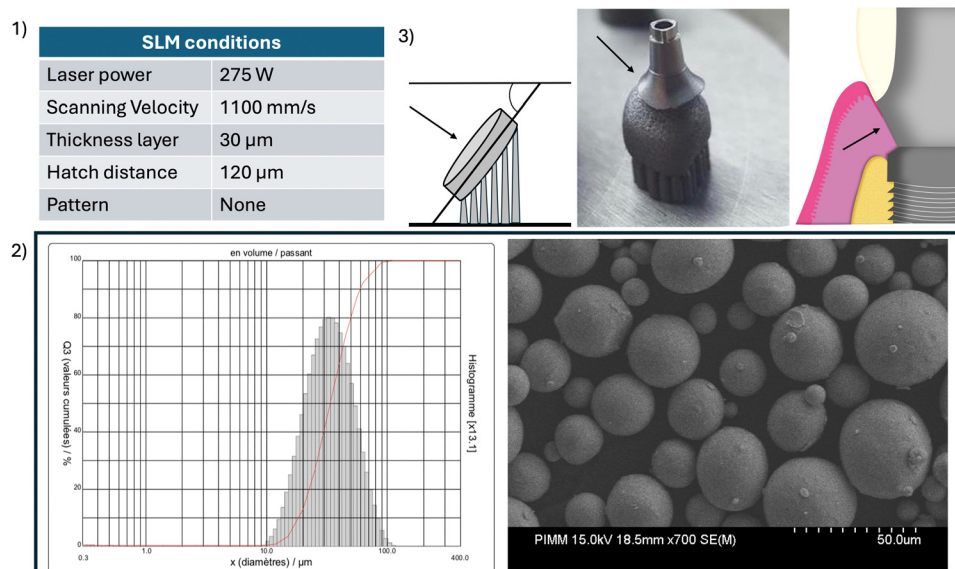
This journal is © The Royal Society of Chemistry 2024

J. Mater. Chem. B, 2024, **12**, 11502–11514 | **11503**

Fig. 1 (1) SLM conditions, (2) particle size distribution and SEM analysis of powder, (3) orientation of the disc during impression compared with a dental printed abutment: the transgingival zone (in direct contact with soft tissues) is intended to be printed at an angle of 30 to 50° to the plate.

diffraction, the American Mineralogist Crystal Structure Database, and the open crystallography database.

As a reference material (control), computer numerically controlled milled (CNCM) specimens were manufactured using an NC 5-axis milling machine (CORiTEC 350i, Imes-Icore) from a titanium alloy grade 5 metal disc (Copra Ti-5, Whitepeaks Dental Solutions GmbH, Wesel, Germany), which is commonly used in milling procedures to achieve implant-supported prosthesis. No postprocessing was performed after milling.

Morphological evaluation of NT growth

Electron backscattered diffraction EBSD. Mechanical polishing was performed on three different SLM discs ($n = 3$) and one reference CNCM disc ($n = 1$), using SiC grinding papers with 320–1200 turning with water, then polished using a SiO_2–H_2O_2 solution, cleaned in acetone for about 10 min and finally dried at room temperature. After polishing, microindentation marks were made to delimit areas of interest by means of a Future-

Tech FM-700 Vickers micro hardness tester. It was decided to construct square patterns with each side 70 μm long (Fig. 2(1)).

On each disc, the most suitable area, *i.e.* free of surface contamination or pollutants, was selected and then mapped using EBSD (electron backscattered diffraction). A field-emission scanning electron microscope (Merlin, Carl Zeiss) was used to collect EBSD maps inside the squares delimited by the nanoindentation marks. The acquisition step (the spatial resolution of the mappings) varied from 50 nm to 200 nm. At 200 nm per pixel, enough points were indexed for α grains, even if the smallest β domains were not resolved. Prior to EBSD analysis, accelerating voltage was set at 20 kV and the stage was tilted at 70°.

Anodization protocol. Specimens were first ultrasonically cleaned in ethanol 70 wt% and deionized water for 5 min each. On the three SLM samples, anodization was performed at constant applied voltages of 10 V, 20 V, and 30 V, respectively, for 1 h using a conventional two-electrode configuration with a platinum foil as the cathode (Fig. 2(2)). The electrolyte solution
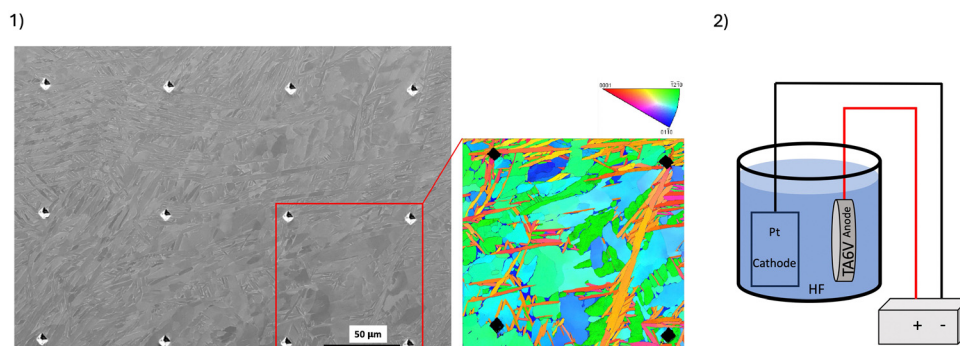

Fig. 2 (1) SEM image showing indentations to identify specific square areas on a SLM sample before anodization. The area marked in red has been chosen for EBSD analysis. (2) Schematization of the anodization system.

11504 | *J. Mater. Chem. B*, 2024, **12**, 11502–11514

This journal is © The Royal Society of Chemistry 2024

was prepared with 50 wt% glycerol, 49.5 wt% distilled water and 0.5 wt% hydrofluoric acid (HF). Then 940 mL of this solution was completed with 60 mL of pure acetic acid (CH₃COOH) solution to get a 1 M concentration, as it has been described that adding CH₃COOH results in more mechanically robust nanotubes without changing their shape or side.[23] The CNCM control sample ($n = 1$) underwent the same procedure at 20 V.

Correlation between EBSD mapping and SEM images. The day after anodization, areas previously mapped by EBSD were identified using the visible indentations on each disc. First, low magnification (1000×) SEM images were acquired using the previously mapped perimeter (Fig. 3(1)), with the accelerating voltage set at 15 kV (Merlin, Carl Zeiss). These SEM images were superimposed on the EBSD images using Photoshop software (version 19.1.6) to correlate the initial microstructure with modified surfaces (Fig. 3(2 and 3)).
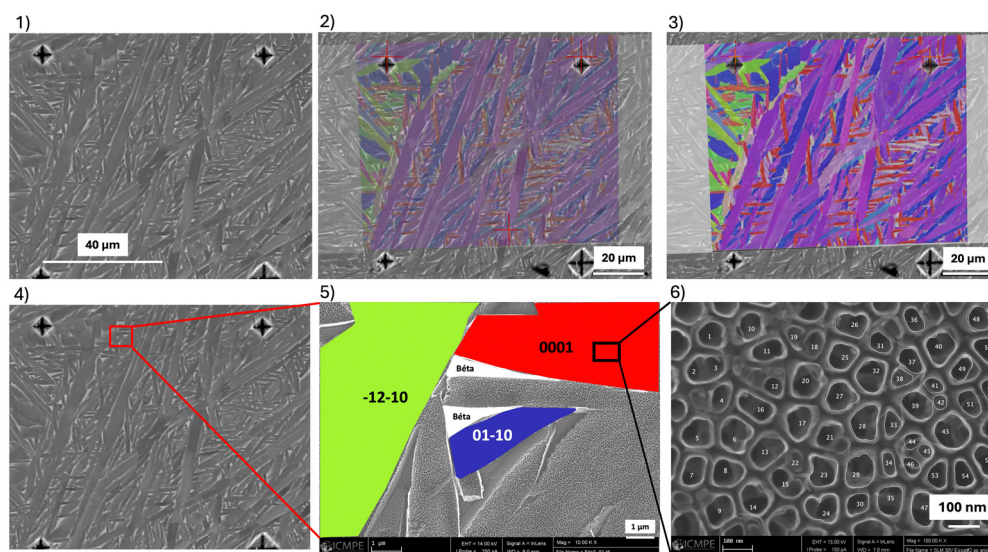
Second, higher magnification images were captured (100.000× and 200.000×) into areas of interest to combine identified crystallographic grains' orientations with the TiO₂ nanotubes' characteristics (Fig. 3(5 and 6)). Energy dispersive X-ray spectroscopy (EDS, Oxford Instruments) maps were used when required to evaluate the chemical distribution. In the case of the visibility of NT, the diameters (for $n = 60$ NTs), the length (for $n = 10$ NTs), and the wall thickness (for $n = 30$ NTs) were measured. Circularity was also analyzed to evaluate the regularity of the tubular structures. Measures were carried out using ImageJ software.

Surface properties evaluation

Before the investigation of surface properties, discs (SLM and CNCM) were mechanically polished (MP), as recommended for prosthetic components in direct contact with gingiva in clinical practice to obtain 2 groups: nine SLM-MP ($n = 9$) and three CNCM-MP ($n = 3$). The polishing steps were first conducted on a

rotational machine using the P240-800-600-1200 sandpaper. Then, all samples were manually polished using a specific dental bur (Dedeco® no. 4950, Long Eddy, NY) inserted in a dental handpiece with a slow speed ranging from 10.000 rpm to 12.000 rpm. And at last, a finishing bur (Robinson Polishing Bristle Brushes soft, Buffalo Dental Manufacturing Co Inc., Syosset, NY) combined with universal polishing paste (Dialux Banc) was applied under the same conditions and all samples were successively ultrasonically cleaned. The nine SLM-MP specimens ($n = 9$) were then anodized following the same protocol as previously described using 3 different voltages (10 V, 20 V, and 30 V) to obtain 3 different sub-groups of three samples: SLM-ANO10 ($n = 3$), SLM-ANO20 ($n = 3$), and SLM-ANO30 ($n = 3$). During the process, the current density curves were recorded using a multimeter device (EmJi Blue®), connected to a dedicated application. CNCM-MP samples were not anodized.

Surface chemical analysis. The chemical composition of the SLM-MP anodized surfaces (for 1 sample per condition, SLM-ANO10, SLM-ANO20, and SLM-ANO30, respectively) was examined using X-ray photoelectron spectroscopy (XPS). A thermo scientific photoelectron K-alpha spectrometer, equipped with a monochromatic Al Kα X-ray source (photon energy = 1486.6 eV), operated at a pressure of around 10^{-9} mbar. The analyzer pass energy was 200 eV for survey spectra and 50 eV for high resolution spectra. The spectrometer was calibrated using Au4f$_{7/2}$ at 84.1 eV and when necessary, energy scale was corrected by referencing the C 1s peak of aliphatic compounds at 285.0 eV. Spectra were recorded and analyzed using Thermo Avantage software that automatically converts peak intensities (counts s^{-1}) into atomic percentages of the different atomic species present in the first few nanometers of the surface layer. A global spectrum (survey) was acquired to calculate the atomic percentages of the various atomic species, and acquisition windows with

Fig. 3 Methodology. (1) After anodization, low magnification SEM images (1000×) and (2) and (3) EBSD maps were superimposed to correlate the microstructure with the modified surfaces. (4) Higher magnification images were captured (100.000×) (6) to correlate the known crystallographic orientation (5) of the substrate with the characteristics of TiO₂ nanotubes.

This journal is © The Royal Society of Chemistry 2024

J. Mater. Chem. B, 2024, 12, 11502–11514 | 11505

better resolution were made to analyze the chemical bonds in which these elements are involved.

Surface roughness. A Bruker Alicona® optical 3D measurement device was used to assess the surface roughness of SLM-MP anodized and CNCM-MP reference discs. For both surface conditions, we measured the profile arithmetic average roughness R_a (arithmetic average of profile height deviations from the mean line) and the corresponding surface roughness parameter S_a (arithmetic average of surface height deviations from the surface) on an 8-mm profile line and a 5-mm² area using MeasureSuite software. Measurements were performed on the three different zones on $n = 3$ discs per condition to consider inter- and intra-specimen variability.

Contact angle. The wettability of the specimens was examined using a drop-shape analyzer (DSA25E Expert, Krüss®, Hamburg, Germany). Water contact angle (CA) was measured by means of the sessile drop method, using a drop of 2 μL of ultrapure distilled water at room temperature (20 °C) and relative humidity (70%). CA was calculated from the profiles of the droplets deposited on the substrates a few seconds after stabilization using the advance software via the ellipse fitting method. Measurements were performed on the three different zones for $n = 3$ discs per condition.

Surface bioactivity evaluation *via* binding collagen

The evaluation of bioactivity of functionalized surfaces has been realized by type 1 collagen adsorption (bovine achilles tendon, C9879 Sigma-Aldrich) with infrared spectroscopy in reflection-absorption mode (IRRAS), using a NICOLET 6700 FTIR spectrometer equipped with a VeeMax accessory enabling reflection–absorption experiments at an incidence angle of 80°. The spectra were averaged over 128 scans and the resolution was set to 4.0 cm⁻¹. The spectrometric system allows the measurement of low concentrations of chemical compounds (simple organic molecules or huge biomolecules) adsorbed onto reflective surfaces such as metals covered with a thin oxide film (passive layer). The application of IR spectroscopy in protein analysis is based on the assessment of the amide bands. These characteristic bands in the infrared spectra of proteins include the amide I, amide II and amide III bands that imply specific vibrations of amide bonds between amino acids. The amide I band appeared in the 1700–1600 cm⁻¹ spectral

range, which is primarily due to the C=O stretch vibrations of the peptide linkages. This is the most intense absorption band appearing in the 1800–1200 cm⁻¹ spectral range. The amide II band (1500–1600 cm⁻¹) as well as the amide III band (1200–1400 cm⁻¹) also had a non-negligible intensity and we choose to correlate the quantity of adsorbed protein with the total intensity of the three former amide bands. The SLM surface anodized at 10 V, 20 V and 30 V, respectively, ($n = 3$ samples per group) soaked in the collagen solution (0.1 g L⁻¹ pH = 8) during 15 min (previously considered as a saturation). Three untreated surfaces ($n = 3$) CNCM-MP were used as the control. After the immersion step, surfaces were flushed with deionized water and sonicated during 5 min. Infrared (IR) spectra were recorded between each step for all the samples and intensities were calculated by the integration of the amide (I, II and III) absorption bands. After sonication, a conductive layer of palladium was applied by sputtering, thanks to a Cressington 208 HR sputter-coater monitored with a Cressington MTM 20 thickness controller. Then SEM images were captured at an acceleration voltage of 15 kV.

Statistical analysis

Data analysis was carried out using Prism software (GraphPad v.10.3.1). To compare diameters and circularity, an ANOVA was used since the number of measurements was equal to 60, assuming a normal distribution of the data. For circularity, a t-test was used. Regarding surface roughness and wettability, Kruskal–Wallis statistical tests were used as the data were not distributed normally (Kolmogorov–Smirnov test). For binding abilities with collagen, an ANOVA was used as the data met the criteria for normality (D'Agostino-Pearson). A $p < 0.05$ was considered significant.

Results and discussion

Phase characterization and crystallographic orientation of surfaces

XRD spectra of the samples are shown in Fig. 4. For the pre-heated group, only peaks associated with the closed-packed hexagonal α phase or α′ phase (hcp) were observed (yellow marks). It has to be mentioned here that a clear difference between α′ and α phases is not possible with the use of XRD as
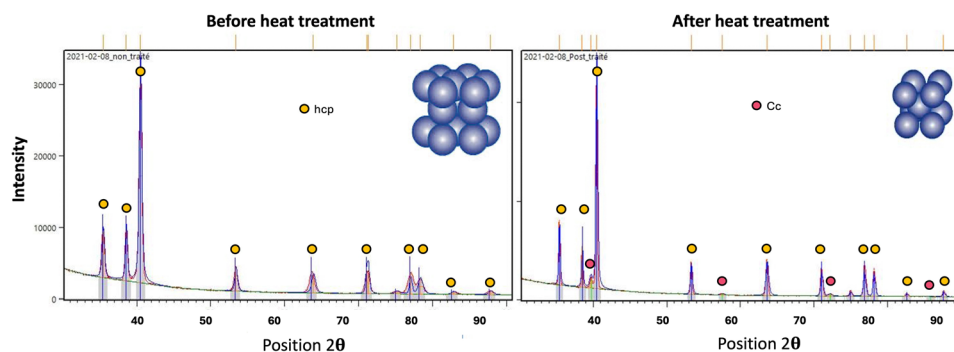

Fig. 4 XRD spectra of SLM samples before and after thermal treatment.

11506 | *J. Mater. Chem. B*, 2024, **12**, 11502–11514

This journal is © The Royal Society of Chemistry 2024

the two hcp crystal lattices are nearly similar. Therefore, we will consider that the microstructure is mostly a martensitic α′ phase, which is usual on as-SLM-built Ti6Al4V. After heat treatment, additional peaks associated with the body-centered cubic β phases (bcc), estimated at 2 wt%, were detected, reflecting the effect of heat treatment. On the CNCM reference sample, the β phase was estimated at 4 wt%.

After HT, a moderate increase in the widths of a'/a laths was observed using EBSD (3.5 μm to 5.1 μm). On the other hand, a clear reduction of the full width at half maximum (FWHM) of X-ray diffraction peaks was noted. This allowed estimating the size of D diffracting crystallites using the Debye–Scherrer equation ($D = K\lambda/(\text{FWHM} \cdot \cos\theta)$). Finally, an average value of 23 nm was obtained for the as built condition compared to 34 nm for the HT material. These two pieces of information (EBSD and XRD) confirm the coarsening of the microstructure after HT.

Fig. 5 shows the four EBSD images before anodization. The SLM samples (Fig. 5(1–3)) showed a mixed microstructure, with both fine lamellar (typical of SLM production) and larger grain structures, which may be quasi-equiaxed (blue in Fig. 5(3)) or more elongated. In contrast, the reference CNCM sample (Fig. 5(4)) had a microstructure with quasi-equiaxed grains, *i.e.* no elongated shape.

Morphological evaluation of NT growth

Influence of microstructure on NT morphology. The α phase was entirely covered with NTs, while the β phase presented "hollow" zones which can qualitatively be associated with dissolution zones (Fig. 6(1)). These observations were made on the SLM specimens and also the CNCM reference sample (Fig. 6(2)). The analysis of the chemical composition *via* energy dispersive X-ray spectroscopy (EDS) carried out in parallel made it possible to confirm the different chemical composition

Fig. 5 EBSD mapping of the four specimen (1)–(3) SLM; (4) CNCM (Reference).

between the 2 phases. The β phase was richer in vanadium and the α phase was richer in aluminum (Fig. 6(3)).

Fig. 7(1) shows SEM images of NTs that have grown on the α phase on the three SLM samples in the top and sagittal views for the three anodizing voltage conditions. On the α phase, the diameter of the NTs increased with the imposed voltage during anodization. Image analysis is used to estimate NTs' diameters (top view), length and wall thickness (sagittal view) (Fig. 7(2–4)).

For a constant anodizing time of 1 h, the inner diameter of the NTs was 35 nm for an anodizing voltage $V = 10$ V, 70 nm for $V = 20$ V, and 98 nm for $V = 30$ V (Fig. 7(2)). In the same way, the length of the NTs increased with voltage. At 30 V, the length was on an average around 400 nm, while it drops to 240 nm at 20 V and 170 nm at 10 V (Fig. 7(3)). Finally, even if the thickness of the walls was very thin and therefore difficult to measure, it was possible to note that the anodizing voltage also influenced the thickness of these walls. These varied from 3 to 9 nm, which corresponds to a fairly small number of TiO_2 molecular layers (Fig. 7(4)). Regarding the TiO_2 NTs formed on the α phase on the control CNCM sample (not shown here), it appeared that the average diameter of the NTs was statistically different compared to the samples obtained by SLM under identical anodizing conditions (83 nm ± 9, 6 *vs.* 69 nm ± 12). The NTs present on the surface of the machined sample were "wider" than those observed on the SLM sample. This difference was also significant concerning the circularity of the NTs: the SLM sample presented less "regular" NTs than those obtained on the control sample (0.89 ± 0.06 *vs.* 0.91 ± 0.04).

Influence of crystallographic orientation on NT morphology. Since no NT had grown on β phase, only the morphology of the NT present on the α phase was analyzed. The SEM micrographs of the appearance of the NTs formed on these crystal planes are presented in Fig. 8. The crystallographic orientation of the HCP lattice relative to the surface of analysis corresponds to the color code (red, blue, green), with the corresponding (0001) = basal plane, 01$\bar{1}$0 = prismatic planes, and ($\bar{1}2\bar{1}0$) = 2nd order prismatic planes. The dimensions of NTs formed by electrochemical anodization were correlated with crystallographic orientations. They were no significant influence of crystallographic orientation on NTs morphology and size at anodizing voltages equal to 20 V or 30 V. However, for an anodizing voltage of 10 V, NTs' diameters were significantly smaller on the basal planes (0001) than on the other planes.

Surface properties

NTs synthesis and electrochemical phenomena. The current transients recorded during anodization for a voltage set at 20 V are shown in Fig. 9(1). The shape of the polarization curves corresponds to the typical behavior for Ti anodization reported for aqueous systems with fluoride additions.[24] After the formation of a compact oxide layer, which is accompanied by a rapid decrease in current, a second distinct peak reflects the action of fluoride ions, which attack this oxide layer creating random pores. This is the initial formation of nanotubes. Finally, the current reaches a stable state, when the pore growth rate at the metal oxide interface and induced dissolution rate of
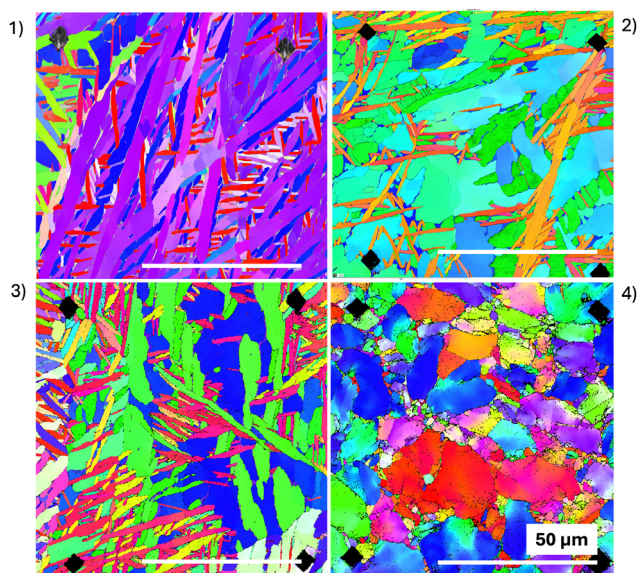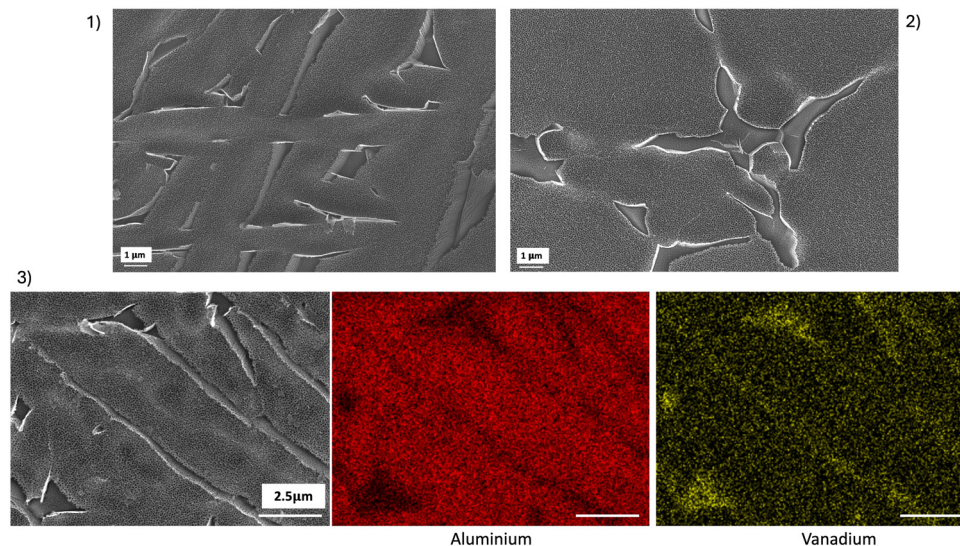
This journal is © The Royal Society of Chemistry 2024

J. Mater. Chem. B, 2024, **12**, 11502–11514 | **11507**

Fig. 6 (1) SEM images after anodization on the SLM sample: NTs grew on the α phase and the dissolution zone was visible on the β phase. (2) The same phenomena were visible on the CNCM control sample. (3) EDS acquisition on the SLM sample: the α phase with NTs showed a more pronounced presence of aluminum (marked in red), while the β phase was richer in vanadium (marked in yellow).
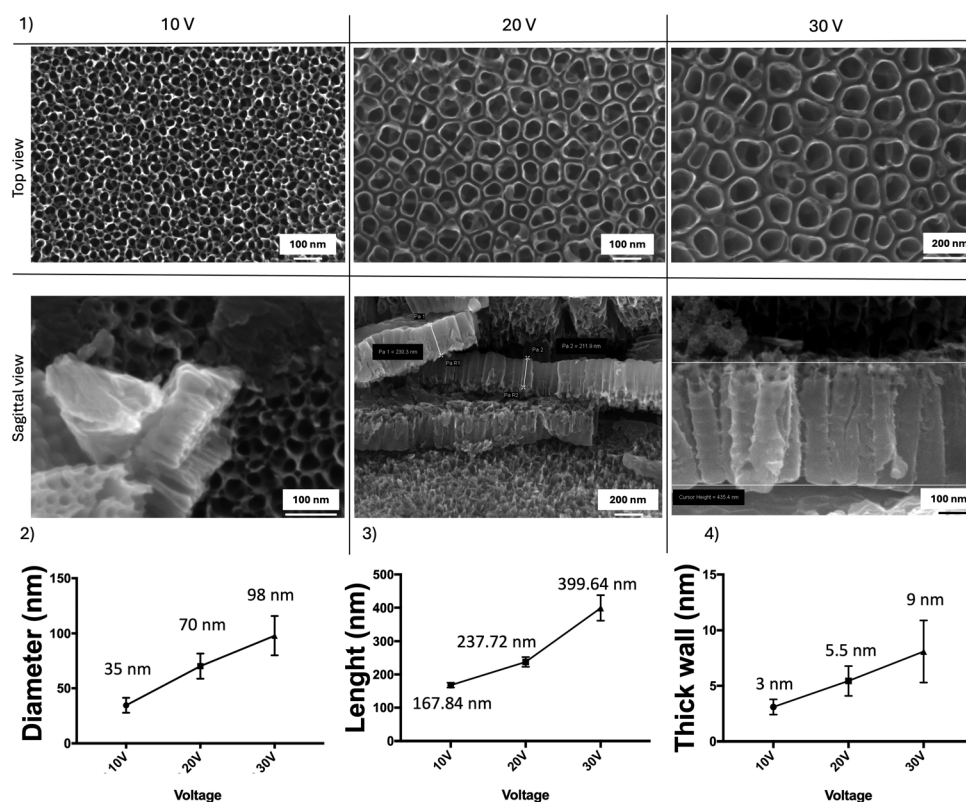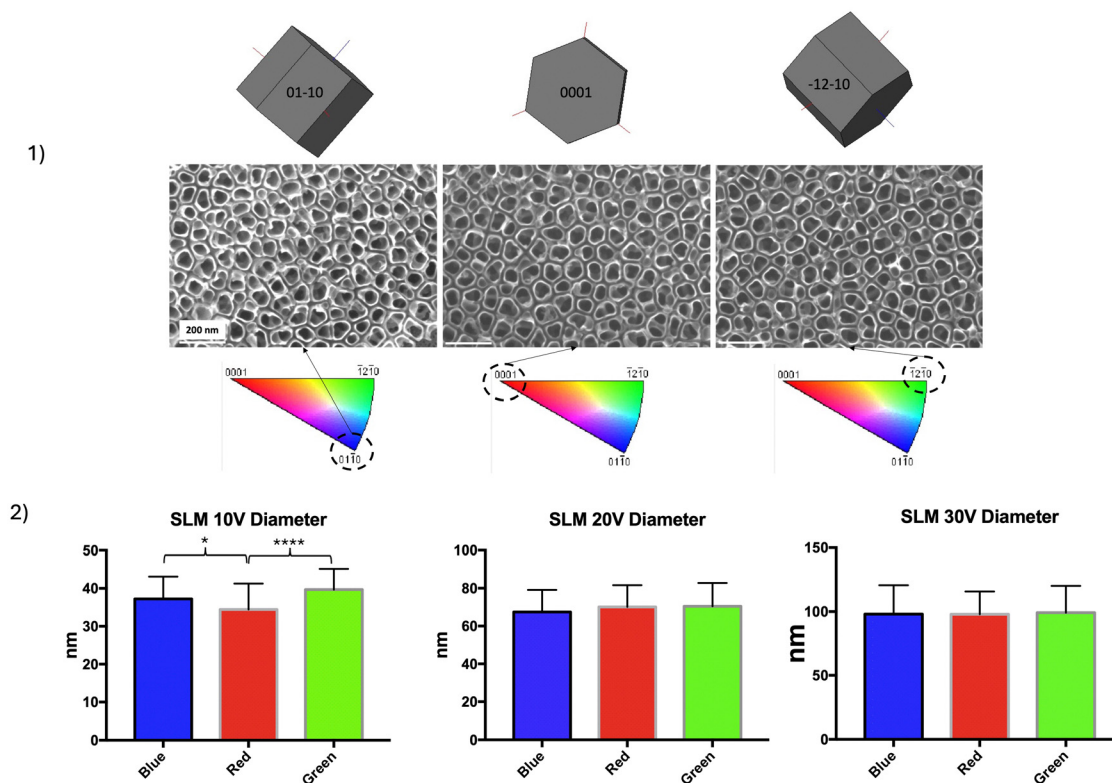

Fig. 7 (1) SEM images showing voltage-dependent nanotube morphology. Influence of applied voltage on (2) the inner diameter, (3) the length, and (4) the thick wall of TiO_2 NTs on SLM specimens.

the formed TiO_2 at the outer interface reach an equilibrium.[7] During this steady stage, self-organized nanotubes (NTs) can grow, and their length is proportional to the anodization time. The anodized SLM surfaces turned pink, while the CNCM-MP control surfaces remained grey (Fig. 9(2)).

Surface chemistry characterization. The XPS spectrum revealed the presence of atomic elements in the first few nanometers of the solid surface, thanks to photopeaks corresponding to element core level lines. Sensibility of XPS is of the order of 0.1 atomic percent and a semi-quantitative

11508 | *J. Mater. Chem. B*, 2024, **12**, 11502–11514

This journal is © The Royal Society of Chemistry 2024

Fig. 8 (1) SEM images of NTs (top view) obtained on different zones on the SLM sample anodized at 20 V. The crystallographic orientation of the HC lattice relative to the surface of analysis corresponds to the color codes red, blue, and green, with the (0001) = basal, (01$\bar{1}$0) = prismatic and ($\bar{1}$2$\bar{1}$0) = pyramidal planes. (2) Mean $\pm$ SD of NTs diameter on zones with different crystallographic orientations for the 3 anodizing conditions. Data were analyzed using an ANOVA test (*$p < 0.05$, ****$p < 0.0001$).
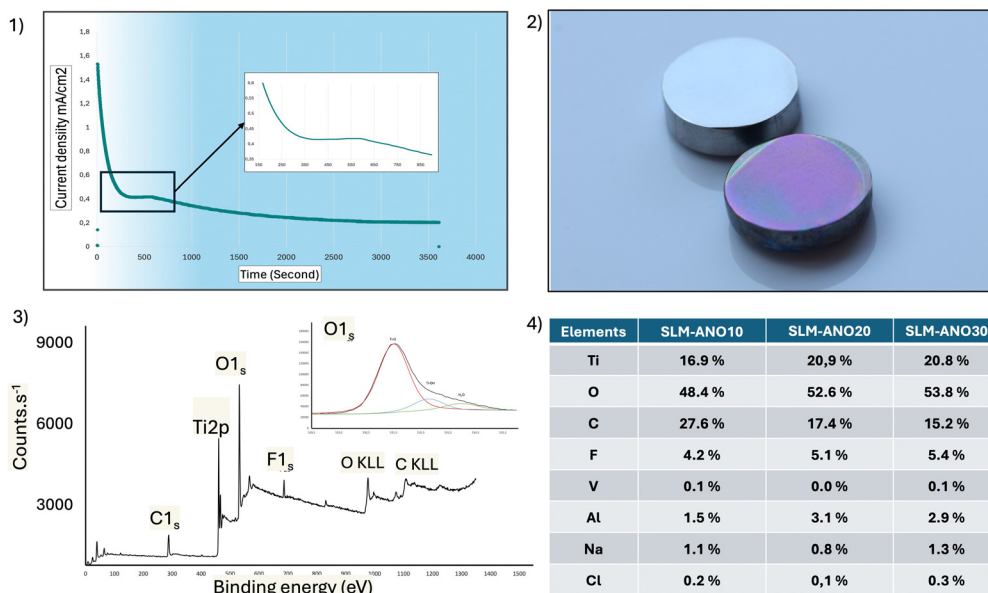
Fig. 9 (1) Typical current density curve recorded for an imposed voltage of 20 V for 1 hour. A zoom reveals the 2nd peak characteristic of an attack on the TiO_2 layer by fluoride ions contained in the electrolyte. (2) SLM-ANO20 disc (in pink) and a CNCM-MP control disc (in silver grey). (3) XPS survey spectrum and O 1s high resolution spectrum (inset) of a freshly anodized SLM-ANO20 sample. (4) Sample composition detected by XPS (at% for $n = 1$).

This journal is © The Royal Society of Chemistry 2024

J. Mater. Chem. B, 2024, **12**, 11502–11514 | **11509**

analysis is possible. Fig. 9(3) shows the survey spectrum of an anodized Ti6Al4V sample (20 V). XPS signal was mainly composed of Ti2p and O 1s peaks with a negligible Al 2p peak. This confirmed that the surface was principally composed of titanium oxide with a very small quantity of aluminum oxide (less than 0.5 at%). Atomic percentages gave a nearly stoichiometric TiO_2 compound with a small excess of oxygen that can be explained by the presence of surface hydroxyls and coordinated species adsorbed onto the surface. This last assertion was validated by the high-resolution O 1s spectrum (inset in Fig. 9(3)), which showed different components corresponding to surface hydroxyls and adsorbed water. Some carbonaceous contamination (C 1s) and fluorine (F 1s) were also identified resulting from the electrolyte bath. The table in Fig. 9(4) shows the percentage of the various elements found on the 3 surfaces for the different voltages imposed. The results show that percentages of the SLM-ANO20 and SLM-ANO30 samples are similar within the bounds of experimental errors. Notable differences are observed, however, when these samples are compared with SLM-ANO10. Carbon contamination is more significant in the latter, which may explain the lower percentage of oxide (approx. 17 at% *vs.* 21 at% Ti). A striking feature of this elemental quantification concerns the percentage of oxygen. The latter reflects enrichment in oxygen compared with the TiO_2 stoichiometry. This observation can reflect the presence of hydroxylated species (hydroxides and water) molecularly adsorbed on the functionalized surface or defective sites.

Roughness and wettability. The mean R_a value was respectively 0.19 ± 0.05 μm, 0.21 ± 0.05 μm, 0.22 ± 0.08 μm and 0.24 ± 0.06 μm for SLM-ANO10, SLM-ANO20, SLM-ANO30 and CNCM-MP. The mean S_a value was respectively 0.22 ± 0.04 μm, 0.28 ± 0.7 μm, 0.25 ± 0.06 μm and 0.29 ± 0.04 μm for SLM-ANO10, SLM-ANO20, SLM-ANO30 and CNCM-MP, with no statistically significant difference between the groups (Fig. 10(1)).

Regarding wettability, anodization impacted the hydrophilic behavior of the titanium surface. SLM-ANO20 and SLM-ANO30 showed a lower water contact angle (38 ± 6° and 46 ± 10°, respectively) than SLM-ANO10 and CNCM-MP (72 ± 7° and 63 ± 6°) and therefore increased hydrophilicity, compared to the MP samples (Fig. 10(2)).

Binding abilities

An example of IRRAS spectra is shown in Fig. 11(1), for SLM-ANO20: (a) extracted from the solution and dried, (b) rinsed with deionized water and dried and (c) after 300 s of sonication in deionized water and dried. IR intensities were calculated by the integration of the amide (I, II and III) absorption bands (sum of peak areas under the curve). The intensity of the absorption bands remained high even after ultrasonic cleaning for 300 seconds. Comparison of IR intensities of the different groups (Fig. 11(2)) showed a little variation in the quantity adsorbed as a function of the anodizing potential. Nevertheless, it seems clear that the quantity of adsorbed collagen was much greater on the anodized samples compared to the control, even after sonication.

The SEM images acquired after sonication (Fig. 11(3 and 4)) confirmed the presence of collagen that remained adsorbed, as measured by IR, showing organic clusters that were not present in the pre-soaking images. Attachment occurred at the edges of the tubes, which leads us to believe that the reactive collagen attachment sites are located at these ends. Nevertheless, a certain quantity of biomolecules penetrated inside the NT. Intermolecular interactions, on the other hand, led to the formation of larger clusters, which appear as bundles in the SEM images.

EA has already been proposed to modify porous Ti6Al4V parts produced by SLM for applications involving contact with bone.[1,14,25] Here we decided to modify a different type of Ti6Al4V surfaces, as our surfaces of interest were manufactured
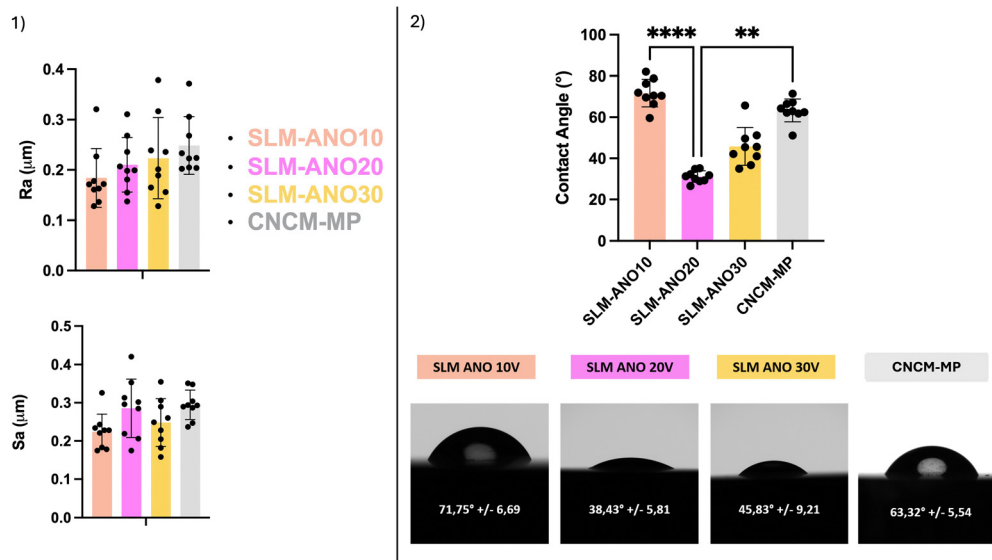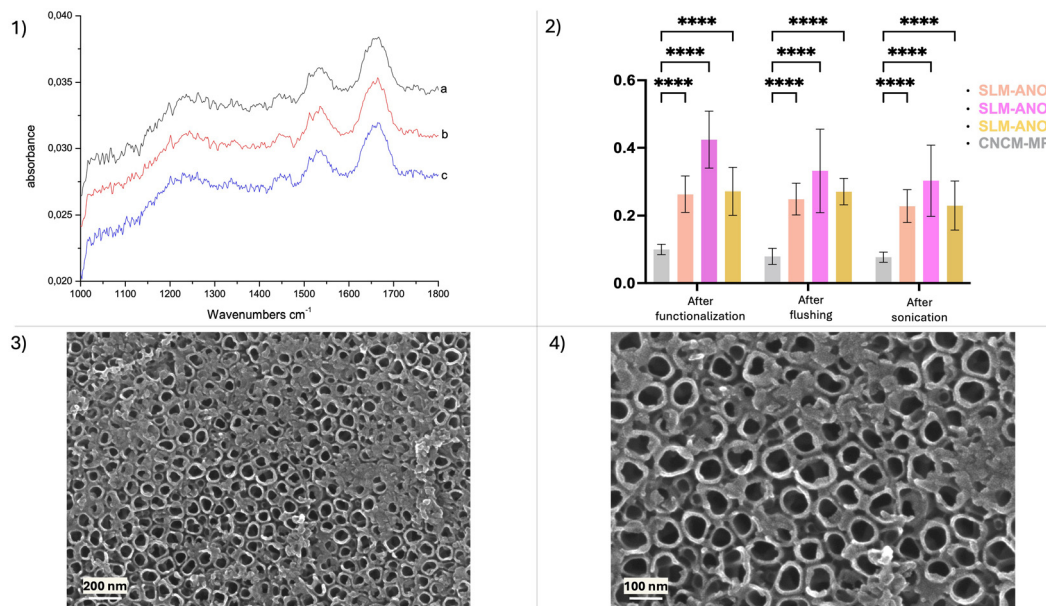

Fig. 10 (1) Average roughness (R_a) and surface average roughness (S_a). (2) Contact angle measurements **** ($p < 0.0001$); ** ($p < 0.005$).

11510 | *J. Mater. Chem. B*, 2024, **12**, 11502–11514

This journal is © The Royal Society of Chemistry 2024

Fig. 11 (1) IRRAS spectra for a SLM-ANO20 sample as extracted from the solution and dried (a), for the sample rinsed with deionized water and dried (b), and for the sample after 300 s of sonication in deionized water and dried (c). (2) Average absorbance of the amide-bond in IRRAS spectra (1778–1415 cm^{-1}) after collagen deposition, after flushing and after sonication ($n = 3$). Rectangles in the histogram represent the IR amide I, II and III intensity as explained in the text ($p < 0.05$). (3) and (4) SEM images of collagen deposition after sonication step ×50.000 and ×100.000.

by copying the protocol used to produce SLM supported-implant prostheses in dentistry. Prosthetic devices differ from implant devices, as porosity is not recommended for the former. Furthermore, the trans gingival area must achieve a $R_a < 0.2$ μm, defined as the threshold that must not be exceeded to avoid bacterial accumulation.[26] When these parts are manufactured by SLM, the settings must be adjusted to obtain dense parts, and after SLM production, pieces received a heat treatment to allow the β phase to appear, giving the parts the ductility required[17] for their application. Then, the laboratory technician preferentially mechanically polishes the trans gingival area (first machined).

Our results show that NTs can form on surfaces obtained by this specific method, but their growth depends on the microstructure. If these observations have already been the subject of rare studies on Ti6Al4V obtained by machining from a cast block, to our knowledge, this is still rarely described for a surface obtained by SLM from a powder of Ti6Al4V.[27] The main hypothesis is correlated with the chemical composition. A potential difference may appear between the α and β phases, to the detriment of the β phase causing its selective dissolution in the reactive medium. This preferential dissolution of β phase must be favored by the size ratio between the fine interstices of β (anodic part) and the majority of large surrounding α grains (cathodic part), which probably increases the dissolution kinetics of β. Since it has been estimated that the β phase corresponds to only 2% of the total surface area of SLM samples through XRD analysis, it is uncertain whether these hollow regions created by cavities would have any clinical impact on gingival cell response. However, it has been described that the β phase can be as high as 25%.[28] In our case, the β phase was present twice the quantity on the control sample obtained by machining a previously cast titanium block (4% vs. 2%). Then, SLM anodized surfaces may therefore offer different site reactions compared to CNCM anodized surfaces.

Regarding the diameter, our values are consistent with those found in the literature: the inner diameter is correlated to the applied voltage.[24] The difference between the SLM and control samples, although minimal, may be linked to the aging of the electrolyte. Indeed, the control sample was treated last and the electrolyte was already used. Aging of the electrolyte can improve the electrochemical phenomena occurring between the surface of the substrate and the electrolyte. Indeed, the pH increases, the conductivity drops, and the ratio of Ti/F ionic species is more favorable to guarantee a more uniform and regular NTs network in an "aged" electrolyte.[29]

For nanotubular growth and its dependence on the grain orientation, it can be concluded that on the HC phase of Ti6Al4V samples obtained by SLM, NTs grow homogeneously and regularly, regardless of the crystallographic orientation of the HC grain or lath, provided the anodizing voltage is greater than 20 V. This difference in diameters between basal and other crystallographic planes at an anodizing voltage of 10 V can be explained by the direct link between surface reactivity and atomic density. In the HC phase, atomic density is higher on a basal plane (red) than on a prismatic plane (blue) or pyramidal plane (green). The greater the atomic density, the lower the surface energy.[30] Thus, the densest basal plane will have the lowest surface energy. It would be expected to be more stable and therefore less reactive. However, above a certain potential, this difference in reactivity between grains may diminish,

This journal is © The Royal Society of Chemistry 2024

J. Mater. Chem. B, 2024, **12**, 11502–11514 | **11511**

thereby masking any crystallographic effects. Other authors have postulated that on basal planes, the natural formation of the oxide layer at the metal–electrolyte interface before NTs formation is dependent on the crystallographic orientation of the underlying grain.[31,32] They report that on basal planes, this layer is denser than on other planes and that, consequently, fluorine ions contained in the electrolyte have difficulty in crossing this barrier, resulting in the non-formation of NTs on these planes.

While manufacturing influences NTs distribution at the nanometric scale, micro roughness is unaffected by EA: there was no statistical difference between the anodized and polished surfaces compared to the polished reference surfaces. The anodized discs all presented an average roughness R_a less than 0.2 μm (Fig. 10(1)) recommended to avoid bacterial infiltration.[26] Hydrophilicity was increased on SLM-ANO20 and SLM-ANO30 compared to SLM-ANO10 and CNCM-MP, with a statistically significant difference between the surfaces anodized at 20 V (SLM-ANO20) and the reference surface (MP-CNCM) (Fig. 10(2)). As we know that wettability affects the first biological response when a medical device is placed into the human body, SLM-ANO20 would therefore have a more suitable surface characteristics to allow protein adsorption to the surface and subsequent interactions with cell receptors[33] Furthermore, SLM-ANO20 presented a mean diameter of 70 nm (Fig. 7(2)) which has been reported in previous work as an ideal diameter to prevent proteins (measuring only a few hundred nm) from falling to the bottom of the tubes and no longer being accessible to the adhesion proteins of the surrounding cells.[9]

Collagen adsorption was used to evaluate how these anodized SLM Ti6Al4V surfaces could interact with protein. Collagen fibers are widely found in peri-implant soft tissues in direct contact with the trans gingival part of abutments, particularly in the connective tissue. Their attachment to the trans-gingival area may provide a barrier to bacteria and their toxins and reduce the risk of peri-implant diseases. In the present work, SLM anodized surfaces showed favorable behavior for collagen adsorption compared to untreated polished CNCM control specimens. Since the intensity of the absorption bands remained high even after flushing and sonication, it may be inferred that the molecules are not simply physisorbed on the edges of the nanotubes, but that strong chemical bonds (electrostatic or covalent) exist between the biomolecules and the nanostructured surface. It is also possible that the collagen remained 'locked' in the spaces between the tubes. Before sonication, collagen seems to be better retained by NTs on SLM-ANO20, but it is extremely difficult to draw any conclusions about the ideal morphology. Indeed, the literature contains discrepancies, and contradictory results emerge depending on the evaluation criteria, *i.e.* optimizing protein adsorption or cell adhesion. Li *et al.* reported that large-diameter TiO_2 nanotubes (<180 nm) exhibit higher protein adsorption, while small-diameter nanotubes are more conducive to cell adhesion, proliferation capacity, and differentiation (20 nm).[34] These results on rat mesenchymal stem cells (MSCs) are consistent with those of Parks *et al.* Who proposed that a 15-nm diameter tub is an optimal diameter to increased cell adhesion and proliferation of

MSCs.[35] However, what is considered ideal for enhancing osteoinduction is unsuitable for promoting gingival cell adhesion. Most studies reporting improved adhesion of gingival fibroblasts to NTs produce diameters in the range of 70 to 100 nm,[10,36,37] similar to those we obtained. Further biological investigations will be required to validate the biological behavior of these 3D-printed titanium surfaces. Finally, assessing the stability of the NT layer is a limitation of this study. This significant aspect requires dedicated mechanical assessments.

The protocol was first applied to previously polished Ti6Al4V surfaces, but NTs also grew on a raw Ti6Al4V surface under the same conditions in terms of chemical composition or crystallography. The resulting surface (Appendix A) exhibits a dual roughness (the surface micro-roughness inherent in the process and the nano-roughness resulting from anodizing).

Conclusions

Ti6Al4V surfaces produced by SLM and then mechanically polished can be anodized in the same way as machined polished Ti6Al4V without affecting surface micro topography. Visually, this translates into the creation of homogeneous NTs on the α phase and the presence of hollow regions on the β phase. Above an applied voltage of 20 V, the diameter, length and wall thickness were not affected by the crystallographic orientation of the underlying metal substrate. To guarantee a homogeneous surface on the α phase and to increase the hydrophilicity of the surface, a protocol including an imposed voltage higher than 20 V seems to be recommended. Collagen strongly attached anodized Ti6Al4V SLM surfaces compared to the polished control which may contribute in the future to optimize the surface bioactivity of trans-gingival components.

Author contributions

Marie-Joséphine Crenn: conceptualization, investigation, data curation, writing, and formal analysis. Lanig Lefort: data curation and investigation. Remy Pires: EBSD and SEM acquisition. Pierre Dubot: resources, investigation, and review & editing. Marie-Laurence Giorgi: review & editing. Patrice Peyre: supervision and validation.

Data availability

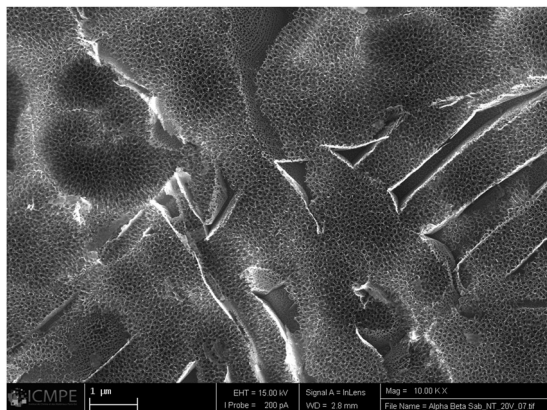The data supporting this article have been included as part of the ESI.†

Conflicts of interest

There are no conflicts to declare.

11512 | *J. Mater. Chem. B*, 2024, **12**, 11502–11514

This journal is © The Royal Society of Chemistry 2024

Appendix A

References

1 S. Demirci, R. Dalmış, T. Dikici, M. M. Tünçay, N. Kaya and A. N. Güllüoğlu, Effect of surface modifications of additively manufactured Ti-6Al-4V alloys on apatite formation ability for biomedical applications, *J. Alloys Compd.*, 2021, **887**, 161445.

2 R. C. S. Silva, A. Agrelli, A. N. Andrade, C. L. Mendes-Marques, I. R. S. Arruda and L. R. L. Santos, *et al.*, Titanium Dental Implants: An Overview of Applied Nanobiotechnology to Improve Biocompatibility and Prevent Infections, *Materials*, 2022, **15**(9), 3150.

3 T. Guo, K. Gulati, H. Arora, P. Han, B. Fournier and S. Ivanovski, Orchestrating soft tissue integration at the transmucosal region of titanium implants, *Acta Biomater.*, 2021, **124**, 33–49.

4 K. Gulati, D. Chopra, N. A. Kocak-Oztug and E. Verron, *Fit and forget*: The future of dental implant therapy via nanotechnology, *Adv. Drug Delivery Rev.*, 2023, **199**, 114900.

5 T. Li, K. Gulati, N. Wang, Z. Zhang and S. Ivanovski, Understanding and augmenting the stability of therapeutic nanotubes on anodized titanium implants, *Mater. Sci. Eng., C*, 2018, **88**, 182–195.

6 A. F. Cipriano, C. Miller and H. Liu, Anodic growth and biomedical applications of TiO_2 nanotubes, *J. Biomed. Nanotechnol.*, 2014, **10**(10), 2977–3003.

7 Y. Fu and A. Mo, A Review on the Electrochemically Self-organized Titania Nanotube Arrays: Synthesis, Modifications, and Biomedical Applications, *Nanoscale Res. Lett.*, 2018, **13**(1), 187.

8 C. von Wilmowsky, S. Bauer, R. Lutz, M. Meisel, F. W. Neukam and T. Toyoshima, *et al.*, In vivo evaluation of anodic TiO_2 nanotubes: an experimental study in the pig, *J. Biomed. Mater. Res., Part B*, 2009, **89**(1), 165–171.

9 M. J. Crenn, P. Dubot, E. Mimran, O. Fromentin, N. Lebon and P. Peyre, Influence of Anodized Titanium Surfaces on the Behavior of Gingival Cells in Contact with: A Systematic Review of In Vitro Studies, *Crystals*, 2021, **11**(12), 1566.

10 Z. Deng, L. Yu, Y. Kuang, Z. Zhou and X. Li, Highly Ordered Nanotube-Like Microstructure on Titanium Dental Implant Surface Fabricated via Anodization Enhanced Cell Adhesion and Migration of Human Gingival Fibroblasts, *Int. J. Nanomed.*, 2024, **19**, 2469–2485.

11 P. W. Garrett, G. W. Johnston, D. D. Bosshardt, A. A. Jones, Y. Sasada and J. L. Ong, *et al.*, Hard and soft tissue evaluation of titanium dental implants and abutments with nanotubes in canines, *J. Periodontol.*, 2020, **91**(4), 516–523.

12 K. Gulati, K. Kant, D. Findlay and D. Losic, Periodically tailored titania nanotubes for enhanced drug loading and releasing performances, *J Mater Chem B*, 2015, **3**(12), 2553–2559.

13 J. Wang, X. T. He, X. Y. Xu, Y. Yin, X. Li and C. S. Bi, *et al.*, Surface modification via plasmid-mediated pLAMA3-CM gene transfection promotes the attachment of gingival epithelial cells to titanium sheets in vitro and improves biological sealing at the transmucosal sites of titanium implants in vivo, *J. Mater. Chem. B*, 2019, **7**(46), 7415–7427.

14 E. Pruchova, M. Kosova, J. Fojt, P. Jarolimova, E. Jablonska and V. Hybasek, *et al.*, A two-phase gradual silver release mechanism from a nanostructured TiAlV surface as a possible antibacterial modification in implants, *Bioelectrochemistry*, 2019, **127**, 26–34.

15 M. F. Kunrath and M. N. Gerhardt, Trans-mucosal platforms for dental implants: Strategies to induce muco-integration and shield peri-implant diseases, *Dent. Mater.*, 2023, **39**(9), 846–859.

16 T. Guo, J. C. Scimeca, S. Ivanovski, E. Verron and K. Gulati, Enhanced Corrosion Resistance and Local Therapy from Nano-Engineered Titanium Dental Implants, *Pharmaceutics*, 2023, **15**(2), 315.

17 M. Benedetti, E. Torresani, M. Leoni, V. Fontanari, M. Bandini and C. Pederzolli, *et al.*, The effect of post-sintering treatments on the fatigue and biological behavior of Ti-6Al-4V ELI parts made by selective laser melting, *J. Mech. Behav. Biomed. Mater.*, 2017, **71**, 295–306.

18 M. J. Crenn, A. Benoit, J. P. Attal and O. Fromentin, Comparison of Mechanical Properties of CAD/CAM-Milled and Selective Laser-Melted Ti-6Al-4V for Dental Superstructures, *Int. J. Prosthodont.*, 2018, **31**(6), 591–593.

19 R. Xu, X. Hu, X. Yu, S. Wan, F. Wu and J. Ouyang, *et al.*, Micro-/nano-topography of selective laser melting titanium enhances adhesion and proliferation and regulates adhesion-related gene expressions of human gingival fibroblasts and human gingival epithelial cells, *Int. J. Nanomed.*, 2018, **13**, 5045–5057.

This journal is © The Royal Society of Chemistry 2024

J. Mater. Chem. B, 2024, **12**, 11502–11514 | **11513**

20 E. Filova, J. Fojt, M. Kryslova, H. Moravec, L. Joska and L. Bacakova, The diameter of nanotubes formed on Ti-6Al-4V alloy controls the adhesion and differentiation of Saos-2 cells, *Int. J. Nanomed.*, 2015, **10**, 7145–7163.

21 Y. Guo, X. Wang, C. Wang and S. Chen, In vitro behaviour of human gingival fibroblasts cultured on 3D-printed titanium alloy with hydrogenated TiO_2 nanotubes, *J. Mater. Sci.: Mater. Med.*, 2022, **33**(3), 27.

22 D. Regonini, C. R. Bowen, A. Jaroenworaluck and R. Stevens, A review of growth mechanism, structure and crystallinity of anodized TiO_2 nanotubes, *Mater. Sci. Eng. R. Rep.*, 2013, **74**(12), 377–406.

23 C. A. Grimes and G. K. Mor, *TiO₂ Nanotube Arrays: Synthesis, Properties, and Applications,* Springer, New York, NY: SpringerLink, 2009 [cité 22 févr 2024]. XXVII, 358. Disponible sur: **https://link.springer.com/book/10.1007/978-1-4419-0068-5**.

24 J. M. Macak, H. Hildebrand, U. Marten-Jahns and P. Schmuki, Mechanistic aspects and growth of large diameter self-organized TiO_2 nanotubes, *J. Electroanal. Chem.*, 2008, **621**(2), 254–266.

25 K. Nune, R. Misra, X. Gai, S. Li and Y. Hao, Surface nanotopography-induced favorable modulation of bioactivity and osteoconductive potential of anodized 3D printed Ti-6Al-4V alloy mesh structure, *J. Biomater. Appl.*, 2018, **32**(8), 1032–1048.

26 C. M. Bollen, P. Lambrechts and M. Quirynen, Comparison of surface roughness of oral hard materials to the threshold surface roughness for bacterial plaque retention: a review of the literature. Dent Mater Off Publ Acad, *Dent. Mater.*, 1997, **13**(4), 258–269.

27 S. Amin Yavari, R. Wauthle, A. Bottger, J. Schrooten, H. Weinans and A. Zadpoor, Crystal structure and nano-topographical features on the surface of heat-treated and anodized porous titanium biomaterials produced using selective laser melting, *Appl Surf Sci*, 2014, **290**, 287–294.

28 W. Xu, E. W. Lui, A. Pateras, M. Qian and M. Brandt, *In situ* tailoring microstructure in additively manufactured Ti-6Al-4V for superior mechanical performance, *Acta Mater.*, 2017, **125**, 390–400.

29 T. Guo, S. Ivanovski and K. Gulati, Tuning electrolyte aging in titanium anodization to fabricate nano-engineered implants, *Surf. Coat. Technol.*, 2022, **447**, 128819.

30 G. Beranger and H. Mazille, Approche scientifique des surfaces. Caractérisation et propriétés, *Tech Ing.*, 2005, 1–21.

31 Z. Su, L. Zhang, F. Jiang, W. Zhou, Z. Deng and Y. Cao, *et al.*, Formation of anodic TiO_2 nanotube arrays with bimodal pore size distribution, *Electrochem. Commun.*, 2013, **31**, 67–70.

32 S. Leonardi, V. Russo, A. Li Bassi, F. Di Fonzo, T. M. Murray and H. Efstathiadis, *et al.*, TiO_2 nanotubes: interdependence of substrate grain orientation and growth rate, *ACS Appl. Mater. Interfaces*, 2015, **7**(3), 1662–1668.

33 R. A. Gittens, L. Scheideler, F. Rupp, S. L. Hyzy, J. Geis-Gerstorfer and Z. Schwartz, *et al.*, A review on the wettability of dental implant surfaces II: Biological and clinical aspects, *Acta Biomater.*, 2014, **10**(7), 2907–2918.

34 Y. Li, S. Wang, Y. Dong, P. Mu, Y. Yang and X. Liu, *et al.*, Effect of size and crystalline phase of TiO_2 nanotubes on cell behaviors: A high throughput study using gradient TiO_2 nanotubes, *Bioact Mater.*, 2020, **5**(4), 1062–1070.

35 J. Park, A. Cimpean, A. B. Tesler and A. Mazare, Anodic TiO_2 Nanotubes: Tailoring Osteoinduction via Drug Delivery, *Nanomaterials*, 2021, **11**(9), 2359.

36 X. Liu, X. Zhou, S. Li, R. Lai, Z. Zhou and Y. Zhang, *et al.*, Effects of titania nanotubes with or without bovine serum albumin loaded on human gingival fibroblasts, *Int. J. Nanomed.*, 2014, **9**, 1185–1198.

37 L. Guida, A. Oliva, M. A. Basile, M. Giordano, L. Nastri and M. Annunziata, Human gingival fibroblast functions are stimulated by oxidized nano-structured titanium surfaces, *J. Dent.*, 2013, **41**(10), 900–907.

11514 | *J. Mater. Chem. B*, 2024, **12**, 11502–11514

This journal is © The Royal Society of Chemistry 2024